INTERNATIONAL JOURNAL FOR NUMERICAL METHODS IN FLUIDS
Int. J. Numer. Meth. Fluids **26**: 907–926 (1998)

A NUMERICAL SOLUTION OF 3D INVISCID ROTATIONAL FLOW IN TURBINES AND DUCTS

ERDAL OKTAY[a,*], İ SİNAN AKMANDOR[b] AND AHMET Ş ÜÇER[c]

[a] *Engineering Development Department, Roketsan, PK40, Elmadag, (06780) Ankara, Turkey*
[b] *Aeronautical Engineering Department, Middle East Technical University, (06531) Ankara, Turkey*
[c] *Mechanical Engineering Department, Middle East Technical University, (06531) Ankara, Turkey*

SUMMARY

The numerical solutions of inviscid rotational (Euler) flows were obtained using an explicit hexahedral unstructured cell vertex finite volume method. A second-order-accurate, one-step Lax–Wendroff scheme was used to solve the unsteady governing equations discretized in conservative form. The transonic circular bump, in which the location and the strength of the captured shock are well predicted, was used as the first test case. The nozzle guide vanes of the VKI low-speed turbine facility were used to validate the Euler code in highly 3D environment. Despite the high turning and the secondary flows which develop, close agreements have been obtained with experimental and numerical results associated with these test cases. © 1998 John Wiley & Sons, Ltd.

KEY WORDS: Euler solvers; finite volume; turbomachinery; duct flow; internal flows

1. INTRODUCTION

At present, several three-dimensional numerical methods can model the flow in turbomachines. An assessment of the 3D internal inviscid codes has been presented by Povinelli [1]. In this paper emphasis has been given to the calculation of secondary flows which develop when initially viscous velocity profiles flow through ducts and blade passages with high turning. Although the geometries treated in these test cases are relatively simple, the high turning coupled with non-uniform inlet conditions create complex flow structures within the computational domain. In the presence of streamwise and normal vorticity components, the flow is highly three-dimensional. The secondary flows result mainly from the motion and the distortion of existing inlet endwall boundary layer. Such mechanisms have been extensively discussed by Sieverding [2]. Since such flows are vorticity dominated, inviscid rotational Euler solvers can successfully predict the flow structure.

To show the versatility and robustness of the presently developed Euler code, test cases involving different internal flow geometries with a wide range of inlet Mach number have been chosen. First, the transonic circular bump problem is solved. At an inlet Mach number of 0.675, the present code successfully places the shock at 72% of the cord. With this test case, the ability of the algorithm to accurately calculate the shock strength and location is illustrated.

* Correspondence to: Engineering Development Department, Roketsan, PK40, Elmadağ(06780) Ankara, Turkey.

CCC 0271–2091/98/080907–20$17.50

Received January 1997
Revised May 1997

The other test case which reports the 3D flow results of the nozzle guide vane of the VKI is also well documented [3–5]. This test case has already been investigated by several researchers [6–8]. Comparison with experiments and other calculations illustrate the capabilities of the present code. As an example, close agreement with the experiment has been obtained in the pitch averaged, tangential flow angles at several axial locations. Therefore, even though comparison between measured and calculated secondary flows in bends and turbine cascades have already been published by other authors, this paper will report numerical results obtained using a second-order-accurate finite volume cell vertex Lax–Wendroff scheme. The present cell vertex scheme uses a directionally independent cell based flux computation technique which is given in the paper. Furthermore, since the Lax–Wendroff scheme is second-order-accurate in time, the distribution of the property changes are modified by higher order terms and the nodes receive an additional corrected flux change. The code has already been validated against 2D subsonic, transonic and supersonic test cases [9,10].

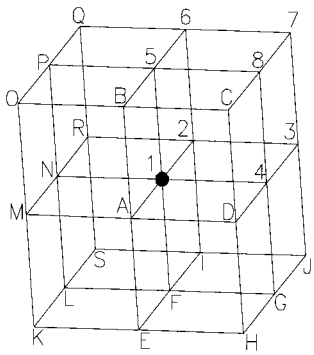

(a) Cells around node 1

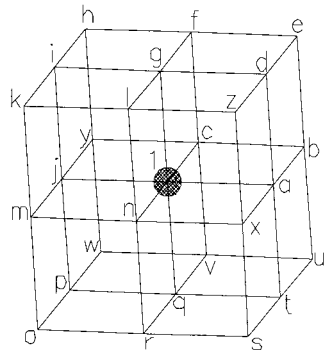

(b) Control volume around node1

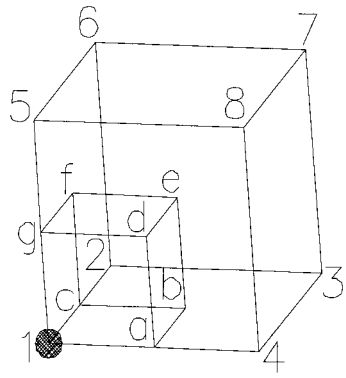

(c) A portion of control volume in cell 1

Figure 1. (a) The cells around node 1; (b) the control volume around node 1; (c) one of the cells bounding node 1.

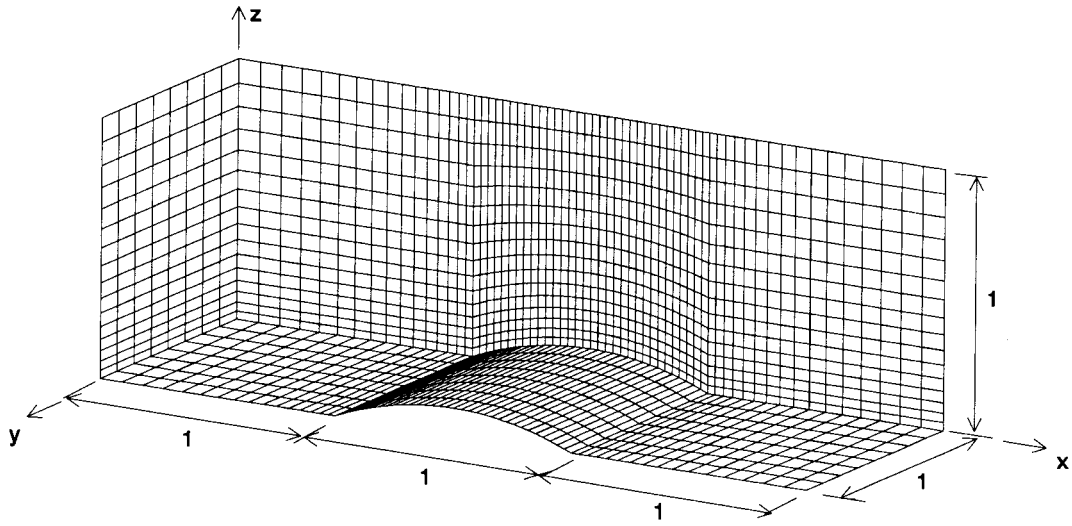

Figure 2. Surface grid of the bump.

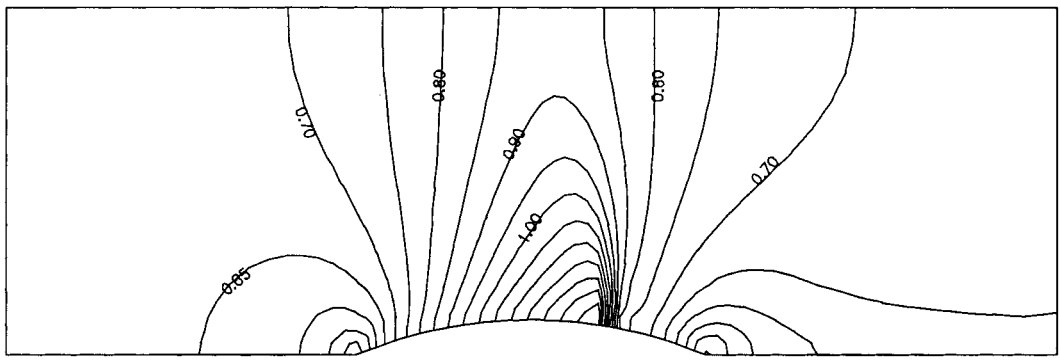

Figure 3. Mach contours on the $y =$ constant planes.

2. GOVERNING EQUATIONS

The system of time-dependent three-dimensional Euler equations are written in integral form using a stationary Cartesian co-ordinate system as:

$$\frac{\partial Q}{\partial t} + \nabla \cdot \bar{\bar{E}} = 0, \tag{1}$$

$$\bar{\bar{E}} = F\vec{i} + G\vec{j} + H\vec{k}, \tag{2}$$

$$Q = \begin{Bmatrix} \rho \\ \rho u \\ \rho v \\ \rho w \\ e \end{Bmatrix} \qquad F = \begin{Bmatrix} \rho u \\ \rho u^2 + p \\ \rho uv \\ \rho uw \\ u(e+p) \end{Bmatrix} \qquad G = \begin{Bmatrix} \rho v \\ \rho uv \\ \rho v^2 + p \\ \rho vw \\ v(e+p) \end{Bmatrix} \qquad H = \begin{Bmatrix} \rho w \\ \rho uw \\ \rho vw \\ \rho w^2 + p \\ w(e+p) \end{Bmatrix}, \tag{3}$$

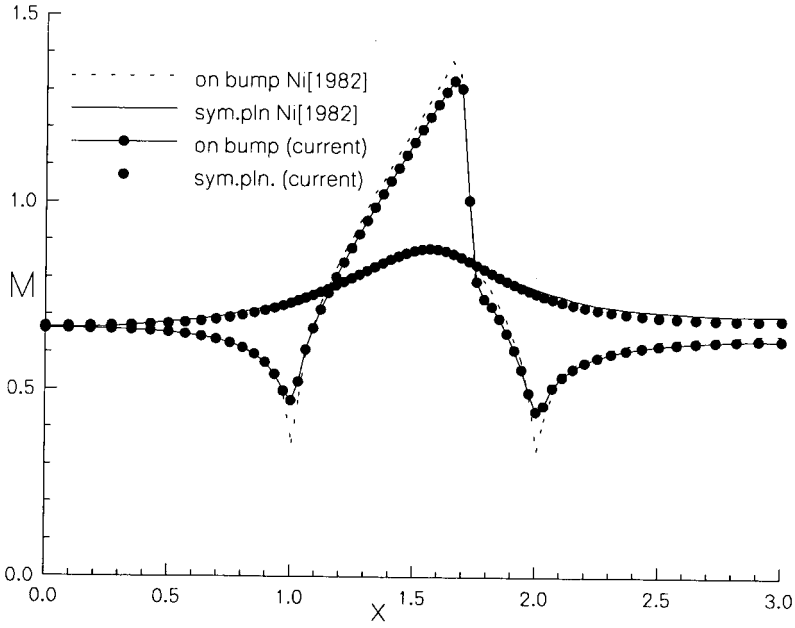

Figure 4. Mach number distribution.

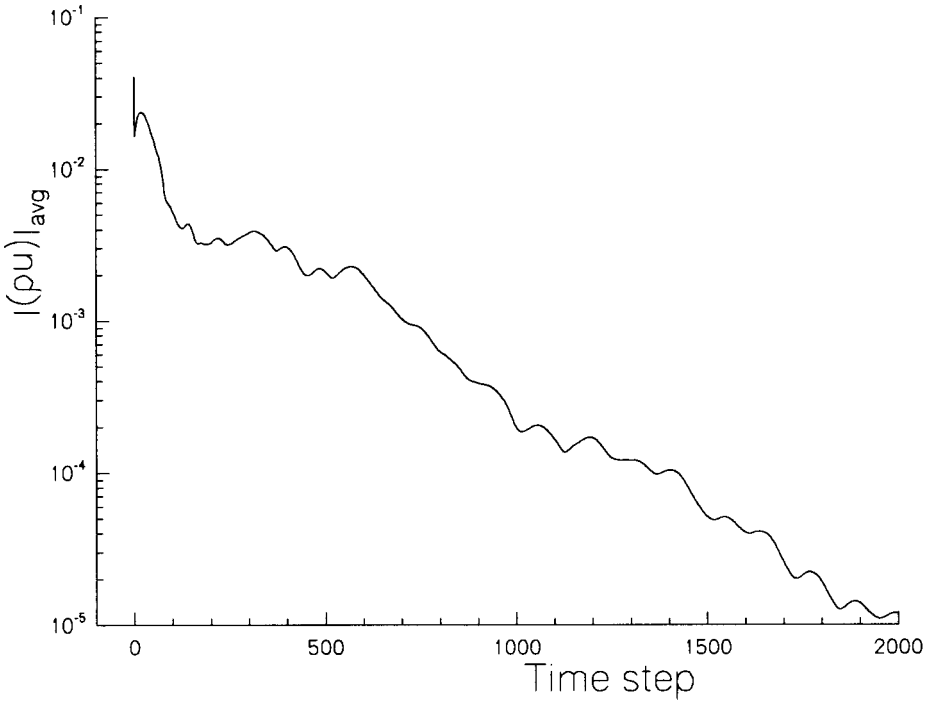

Figure 5. Convergence history.

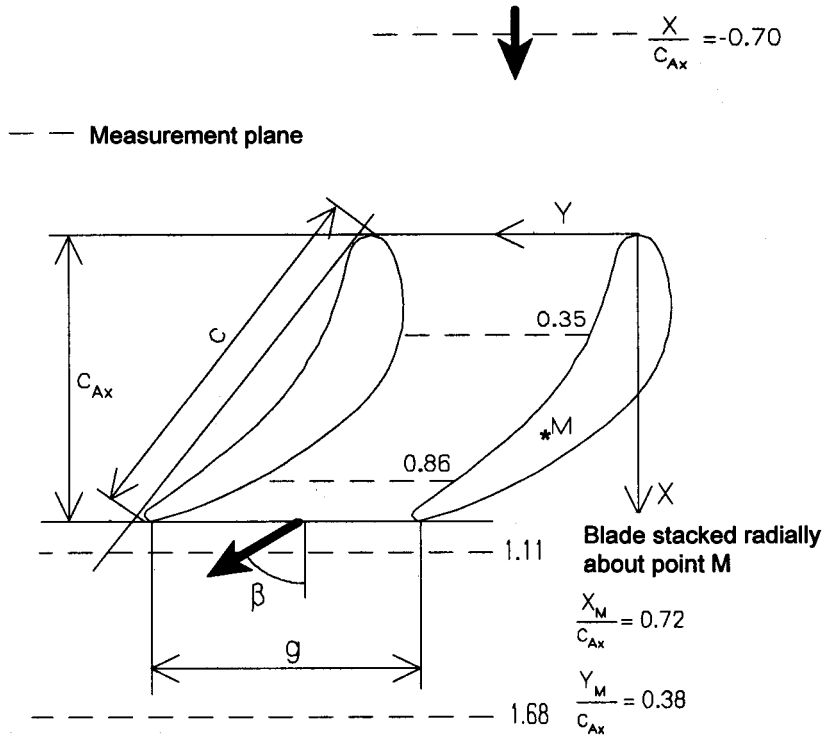

Figure 6. Blade-to-blade geometry at mid-blade hide.

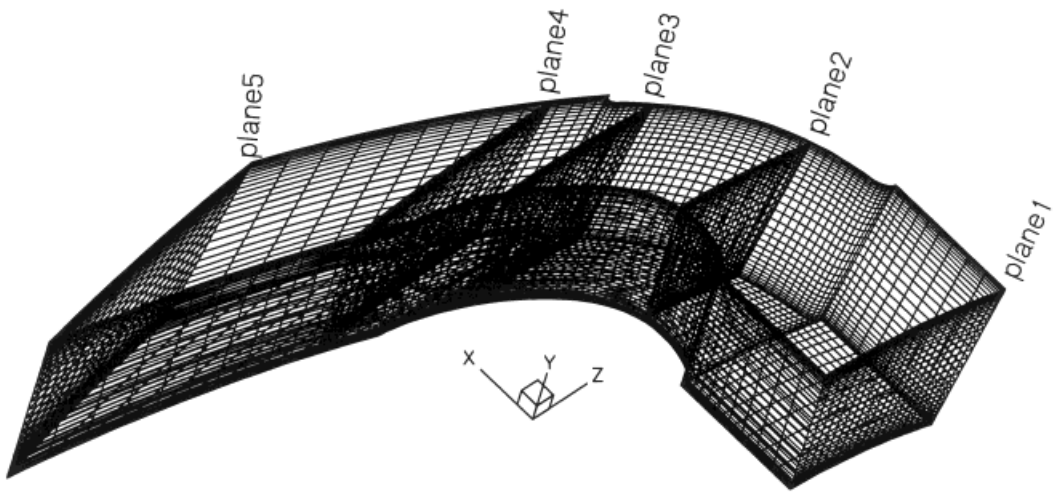

Figure 7. Surface grid with measurement planes.

$$p = (\gamma - 1)\left[e - \frac{1}{2}\,\rho(u^2 + v^2 + w^2) \right]. \tag{4}$$

3. DISCRETIZATION OF GOVERNING EQUATIONS

A second-order-accurate one-step Lax–Wendroff type integration scheme due to Ni [11] has been employed to discretize the Euler equations. The solution at any grid point m, at time level $n+1$, can be expressed in terms of the solution at time level n using a Taylor series expansion.

$$Q_m^{n+1} = Q_m^n + \left(\frac{\partial Q}{\partial t}\right)_m^n \Delta t + \left(\frac{\partial^2 Q}{\partial t^2}\right)_m^n \frac{\Delta t^2}{2} + O(\Delta t^3). \tag{5}$$

From Equations (1) and (5):

$$Q_m^{n+1} = Q_m^n - \nabla \cdot \bar{\bar{E}} \Delta t - \left(\nabla \cdot \frac{\partial \bar{\bar{E}}}{\partial t}\right) \frac{\Delta t^2}{2}. \tag{6}$$

By defining $(\partial E/\partial t)\,\Delta t = \Delta \bar{\bar{E}}$

$$Q_m^{n+1} = Q_m^n - \nabla \cdot \bar{\bar{E}} \Delta t - \nabla \cdot \Delta \bar{\bar{E}} \frac{\Delta t}{2}, \tag{7}$$

where $\Delta \bar{\bar{E}} = \Delta F \vec{i} + \Delta G \vec{j} + \Delta H \vec{k}$.

Integration of Equation (1) using Equation (6) and divergence theorem gives:

$$Q_m^{n+1} = Q_m^n - \frac{\Delta t}{\Delta V} \iint_{\partial\Omega} \bar{\bar{E}} \cdot \mathrm{d}\vec{s} - \frac{\Delta t}{2\Delta V} \iint_{\partial\Omega} \Delta \bar{\bar{E}} \cdot \mathrm{d}\vec{s}. \tag{8}$$

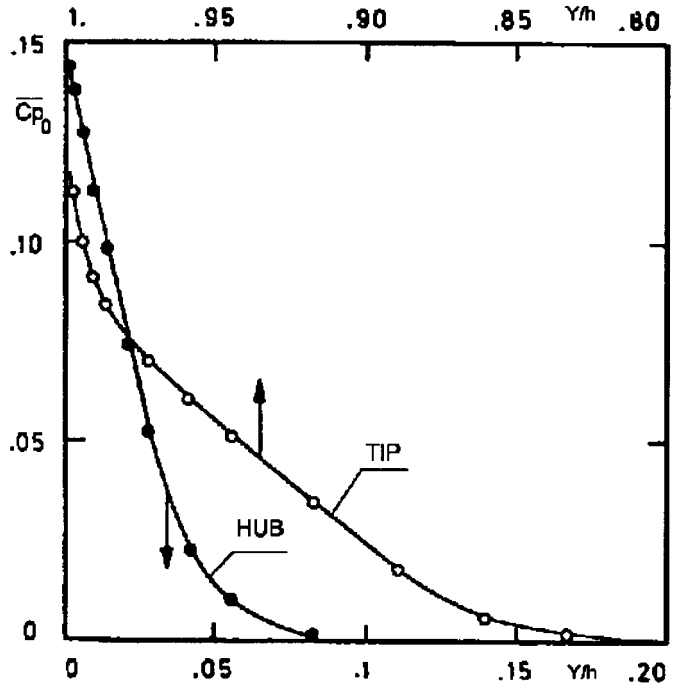

Figure 8. Upstream total pressure loss distribution [4].

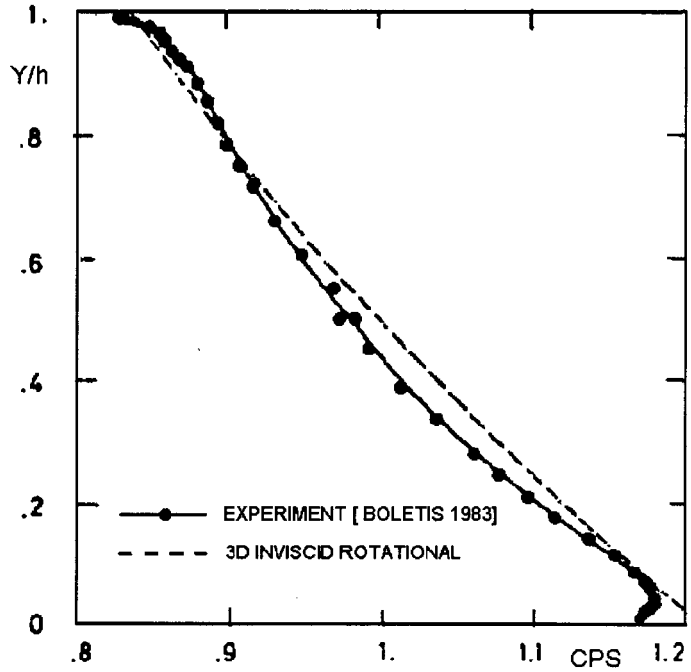

Figure 9. Downstream radial static pressure distribution [4].

Figure 1(a) shows eight cells around node 1. Figure 1(b) depicts the control volume around node number 1. Figure 1(c) shows one of the cell bounding node 1 and 1/8 of the control volume.

The first integral in Equation (8) is evaluated around the cell in Figure 1(c) as follows:

$$\Delta Q = -\frac{\Delta t}{\Delta V}\sum_{i=1}^{6}(F_i S_{ix} + G_i S_{iy} + H_i S_{iz}). \tag{9}$$

Here i represents the face number of the cell, S is the surface vector, and from Equation (1),

$$\Delta Q = -\left(\frac{\partial Q}{\partial t}\right)\Delta t = -\Delta t \nabla \cdot \bar{\bar{E}}. \tag{10}$$

F, G and H in Equation (9) are calculated on the faces of the cell by averaging the flow properties of four nodes defining the considered face. Expressions for S vectors are given in Appendix C.

Control volumes are created by dividing each cell (12345678), into eight small hexahedrons (1abcdefg in Figure 1(c)). This division is carried out by connecting the mid-points of edges, face centroids and centroid of the cell. The second integral in Equation (8) is taken around the control volume (owuskhez in Figure 1(b)) which encloses the considered node point

$$\iint_{\partial\Omega} \Delta\bar{\bar{E}}\, \mathrm{d}s = \sum_{i=1}^{6}(\Delta F_i s_{ix} + \Delta G_i s_{iy} + \Delta H_i s_{iz}), \tag{11}$$

where s_i represents the surface area vector related to the control volume. It is approximated as 1/4 of the respective cell face.

$$\Delta F = \frac{\partial F}{\partial Q}\Delta Q, \qquad \Delta G = \frac{\partial G}{\partial Q}\Delta Q, \qquad \Delta H = \frac{\partial H}{\partial Q}\Delta Q. \tag{12}$$

ΔF, ΔG and ΔH in Equation (12) are given in Appendix B.

Thus, Q vector at the node number m, at time step $n+1$ is calculated as:

$$Q_m^{n+1} = Q_m^n + \frac{1}{8}\left\{\Delta Q + \frac{\Delta t}{\Delta V}\left[\sum_{i=1}^{6}(\Delta F_i s_{ix} + \Delta G_i s_{iy} + \Delta H_i s_{iz})\right]\right\}. \tag{13}$$

A comprehensive description of the method is given by Oktay [9,10].

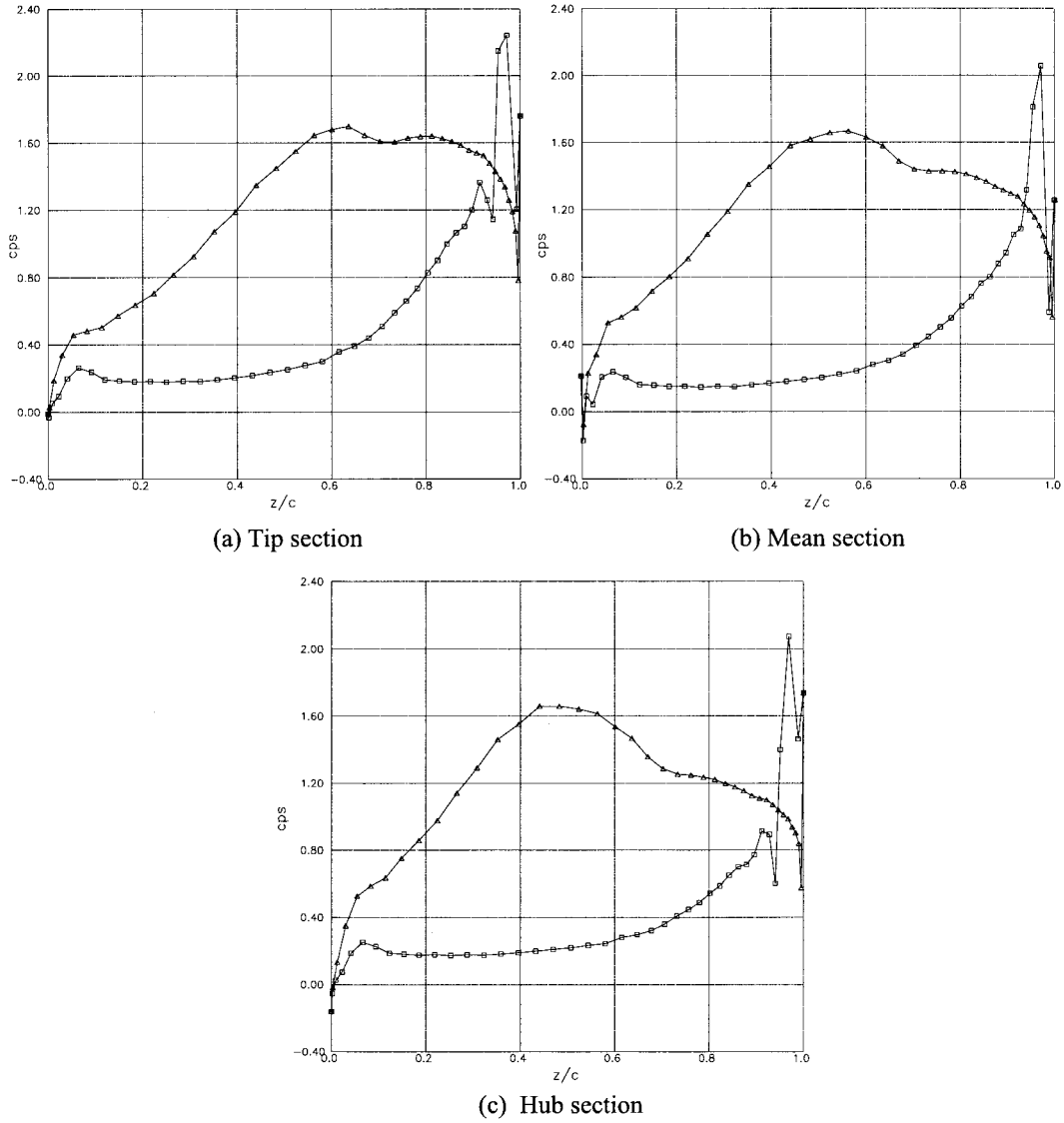

Figure 10. C_p distributions at various sections.

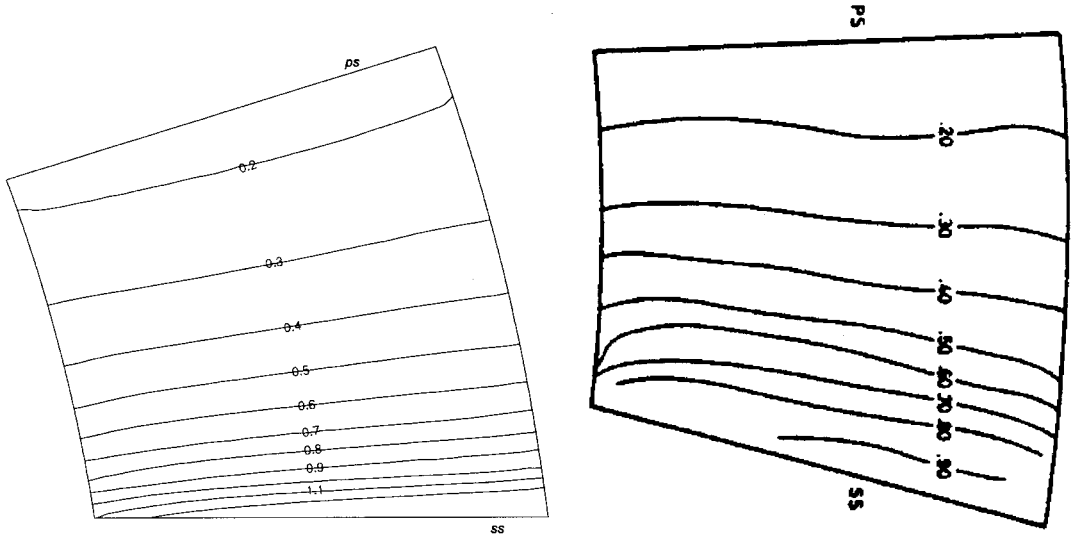

(a) $x/c_{Ax} = 0.35$ Computational Experimental [4]

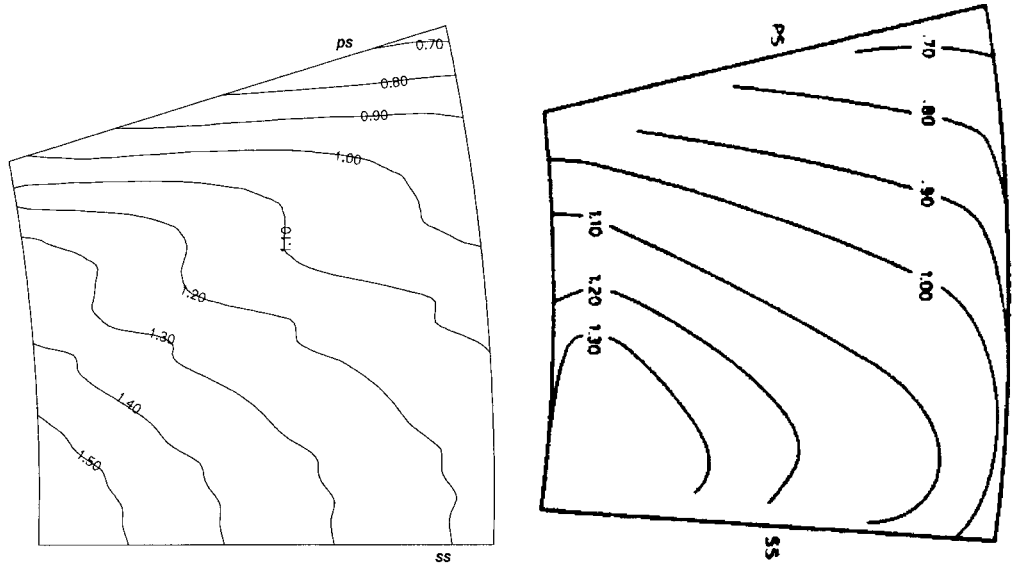

(b) $x/c_{Ax} = 0.86$ Computational Experimental [4]

Figure 11. Contour plots of static pressure at various planes.

4. BOUNDARY CONDITIONS

At the inlet, total temperature $T_{0\text{ref}}$ is specified as constant. The non-uniform inlet condition is obtained by supplying $P_0/P_{0\text{ref}}$ as imposed by the inlet boundary layer. For irrotational flow, $P_0/P_{0\text{ref}}$ is taken as uniform at the inlet. Flow angles β and γ are specified as zero. For all the test cases in this paper, β and γ are taken as zero. For subsonic flows, the inlet conditions are found by extrapolating the upstream running Riemann invariant. All other upstream variables are calculated using Equation (14), the isentropic relations and the specified total pressure variation.

$$V = \frac{(k-1)R^- + \sqrt{2(1-k)(R^-)^2 + 4(k+1)C_p T_{0ref}}}{(k+1)}. \tag{14}$$

For subsonic outflow, the exit static pressure is specified and other variables are taken from the computational domain. For annular geometries, the hub pressure is specified and the radial pressure distribution is calculated by integrating the axisymmetric radial momentum equation. At solid wall boundaries, the tangency condition is used. Pressure and density are calculated from the inner nodes using the method of characteristics. Solutions at nodes on the periodic boundaries are treated as if they were internal nodes, specifying the addresses of cells which are in flux interrelation.

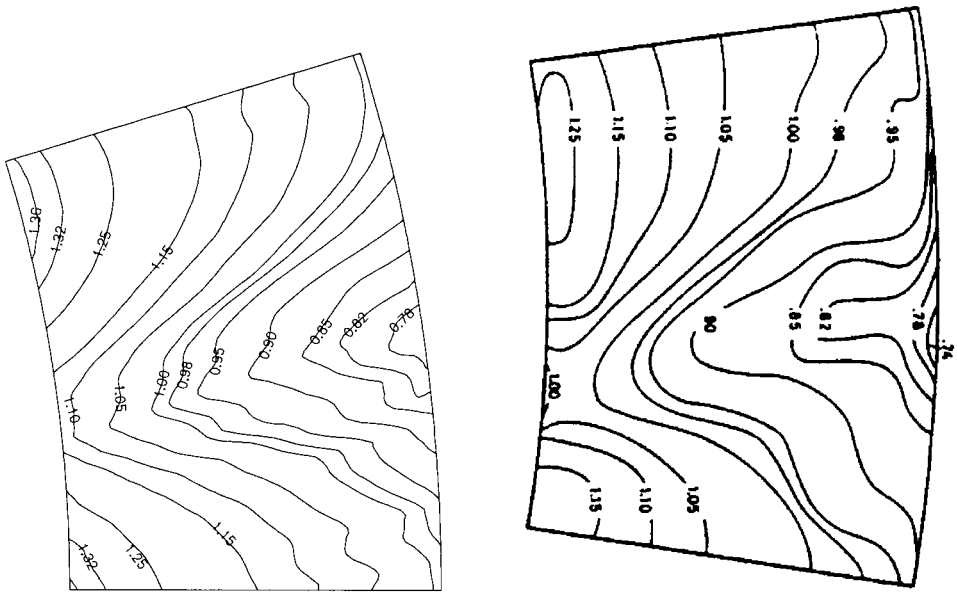

(c) $x/c_{Ax} = 1.11$ Computational Experimental [4]

Figure 11 (*Continued*)

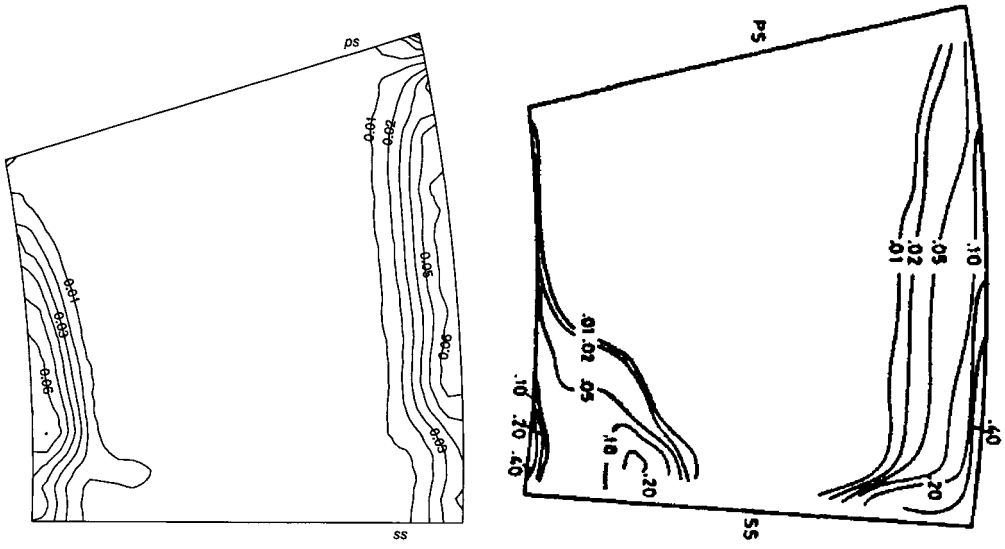

Figure 12. Contour plot of total pressure loss $x/c_{Ax} = 0.86$.

5. NUMERICAL SMOOTHING

Although numerical smoothing is an unavoidable requirement for time marching Euler solvers to stabilize the solution for transonic and supersonic flows, it is also needed in the case of subsonic problems which contain grid non-uniformities.

In this work, a numerical smoothing model is used by adding a smoothing term into the right-hand-side of Equation (13):

$$Q^n_{\mathrm{smt}} = 0.125\mu(Q^n_c - Q^n_m), \tag{15}$$

where Q^n_{smt} is the smoothing operator and $Q^n_c$is the average of Q at surrounding nodes of the cell. Successive application of the smoothing operator results in second-order smoothing.

$$\mu = \sigma \frac{\Delta t}{\Delta V} \sum_{i=1}^{3} \mathrm{d}l_i, \qquad \mathrm{d}l_i = \sqrt{S^2_{ix} + S^2_{iy} + S^2_{iz}}, \qquad 0 < \sigma < 0.1. \tag{16}$$

Here, S_{ix}, S_{iy} and S_{iz} are surfaces of the local co-ordinate system which pass through the cell center. Subscripts x, y and z represent projected areas of these surfaces in the respective directions. In this paper, σ is taken as 0.07 for transonic cases and 0.001 for low subsonic cases.

6. LOCAL TIME STEPPING

Local time stepping accelerates convergence to steady state by advancing the solution at each cell in time at a CFL number near the stability limit. The time step is calculated from:

$$\Delta t = \mathrm{CFL} \times \Delta V \times \min(S_{ix}u + S_{iy}v + S_{iz}w + a\sqrt{S^2_{ix} + S^2_{iy} + S^2_{iz}}), \quad i = 1, 3. \tag{17}$$

7. RESULTS AND DISCUSSION OF THE TEST CASES

7.1. Transonic circular bump

The channel geometry is constructed of a 10% thick circular arc bump at the bottom of the flow domain with the other sides being planer. The 3D $65 \times 9 \times 17$ (streamwise $\times$ pitchwise $\times$ spanwise) algebraic grid is generated by stacking the 2D grid on the xz co-ordinate plane through the spanwise y-direction (Figure 2). This grid is generated by stretching through the streamwise and spanwise directions.

The problem is initiated from a uniform flow. At the inlet, total temperature, total pressure and flow angles ($\alpha = 0.0$, $\beta = 0.0$) are specified. At the exit, static pressure corresponding to Mach number $= 0.675$ is specified.

The location of the shock at 72% of the chord from the leading edge (Figure 3 and Figure 4) and the strength of the shock are in very close agreement with the original solution of Ni [11]. A sharp shock is obtained without any over or undershoots. Three and a half orders of convergency is achieved within 2000 iterations (Figure 5)

7.2. The nozzle guide vanes of the VKI low-speed turbine

7.2.1. Description of the problem. The test case is a low speed ($V_{\text{inlet}} = 12.5$ m s^{-1}), low aspect ratio (height/chord $= 0.6$), high turning (65° from axial direction) annular nozzle guide vane [3,5]. The investigated guide vane has a uniform profile over the spanwise direction and is untwisted (Figure 6). Although the geometry is relatively simple, the two-dimensional inlet flow with collateral inlet endwall boundary layer develop into a full three-dimensional flow within the blade passage. There are two main reasons for this: first, the existence of the inlet vortices pointing toward the blade to blade direction; and second, the highly uneven blade

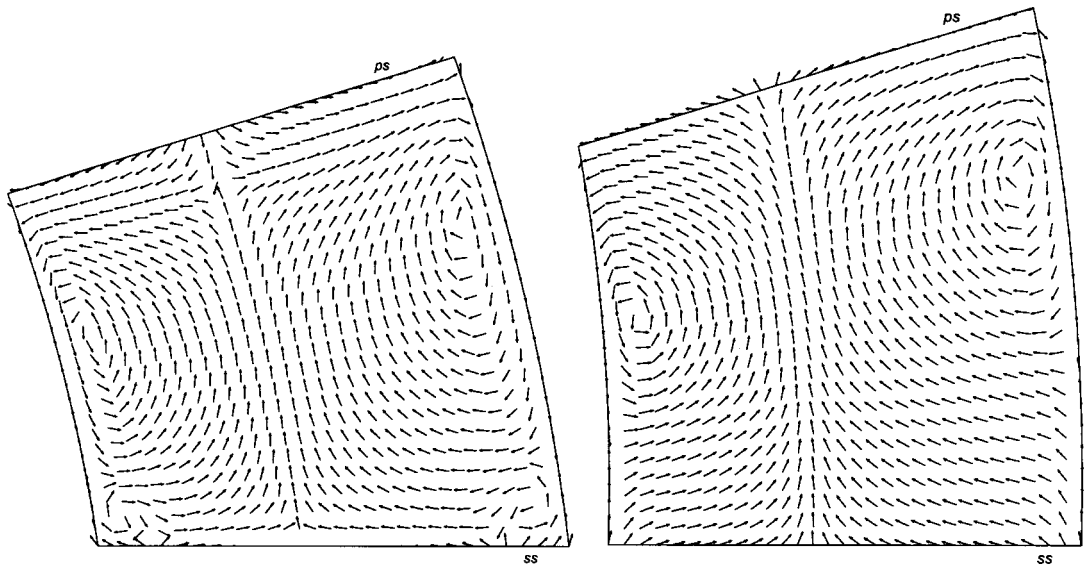

Figure 13. Secondary velocities at various measurement planes.

loading due to high turning in the circumferential direction in an annular blade passage. Hence, two vortical mechanisms can be discerned:

- Two horse-shoe vortices hanging at the leading edge of the blades at the hub and tip and the stretching in the streamwise direction along the blade suction and pressure sides.
- The development of two counter rotating passage vortices, also caused by the radially non-uniform inlet flow condition and enhanced by 3D blade loading. The inlet total pressure endwall boundary layer was specified over 21 points in the radial (spanwise) direction.

An algebraic $66 \times 21 \times 31$ (streamwise $\times$ pitchwise $\times$ spanwise) grid was generated using IDEAS™. This grid is presented in Figure 7.

7.2.2. Inlet and exit boundary conditions. At the inlet, the flow is purely axial ($\beta = 0$ and $\gamma = 0$). A constant total temperature T_0 distribution and a spanwise endwall total pressure profile is determined from the pressure loss distribution given by Boletis (Figure 8) which is uniform in the pitchwise direction. At the exit plane, the static pressure is fixed at the hub. The value of the hub pressure corresponds to an isentropic outlet Mach number of 0.3. This Mach number, higher than the experimental value by one order, was chosen to enhance convergence as suggested by Arts [6] and Novak *et al*. [8]. The spanwise distribution of the pitchwise averaged static pressure coefficient at the exit is obtained using the radial momentum equation. Figure 9 shows this static pressure distribution and the corresponding experimental results [4]. Three and a half orders of convergency are reached after 8000 iterations for this test case.

7.2.3. Static pressure results. Variations of the static pressure coefficient on blade surfaces are given in Figure 10(a)–(c). At the trailing edge of the blade profile, a non-physical over expansion is observed. The flow model is inviscid and no viscous modeling has been carried

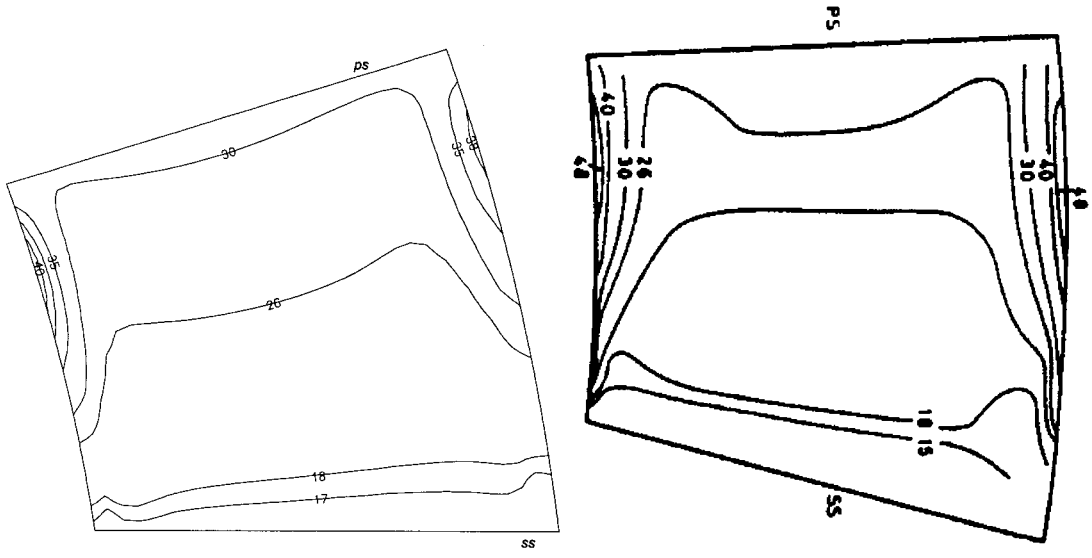

(a) $x/c_{Ax} = 0.35$ Computational Experimental [4]

Figure 14. Contour plots of flow angle β at various measurement planes.

out in this zone, therefore high values and oscillations are expected (Figure 10(a)–(c)). Static pressure contours given at $x/c = 0.35$, as shown in Figure 11(a) show that the variation is mainly from pressure side to suction side and exhibit a typical 2D pitchwise pressure gradient. Further downstream at $x/c = 0.86$ (Figure 11(b)), high turning and secondary flow effects shift the direction of the static pressure gradient. Just outside the blade passage $x/c = 1.11$ (Figure 11(c)), the trailing edge of the blades is clearly marked with 'V'-shaped contours. Close

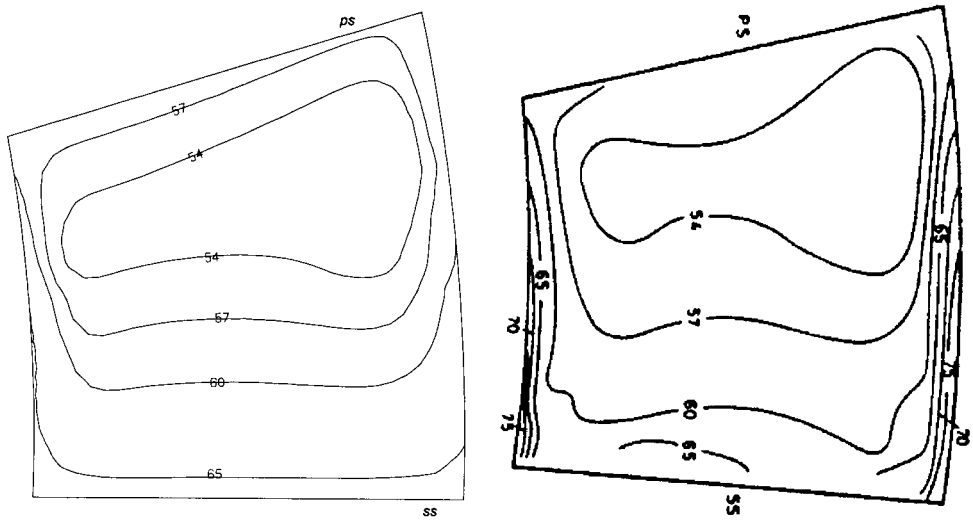

(b) $x/c_{Ax} = 0.86$ Computational

Experimental [4]

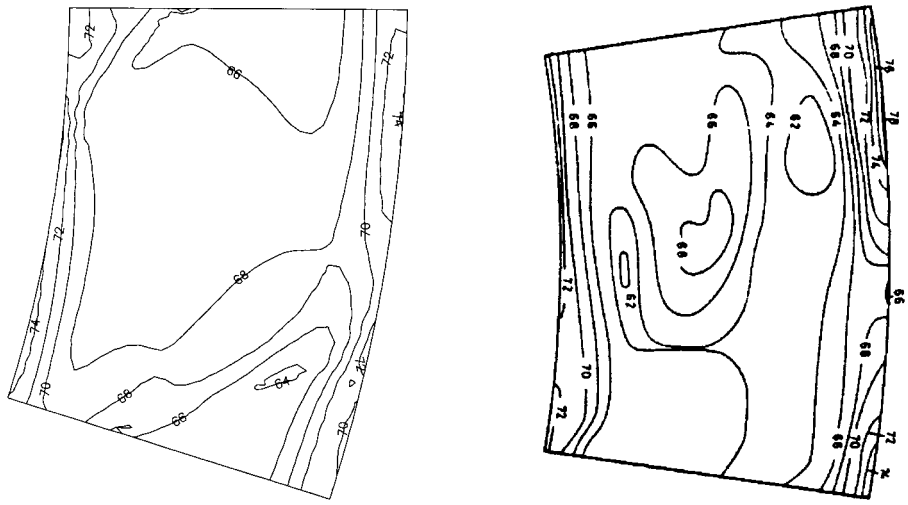

(c) $x/c_{Ax} = 1.6$ Computational

Experimental [4]

Figure 14 (*Continued*)

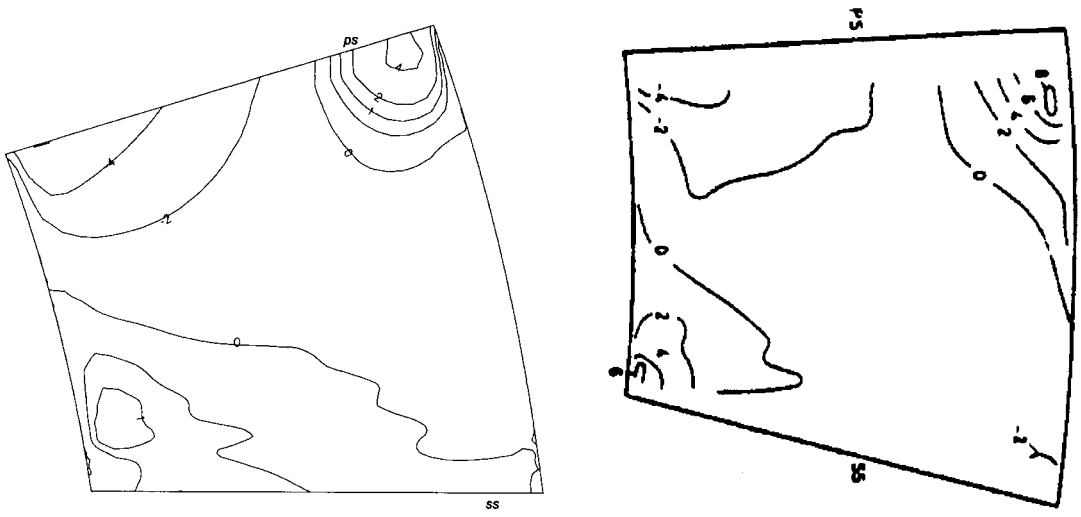

(a) x/c_{Ax}=0.35 Computational Experimental [4]

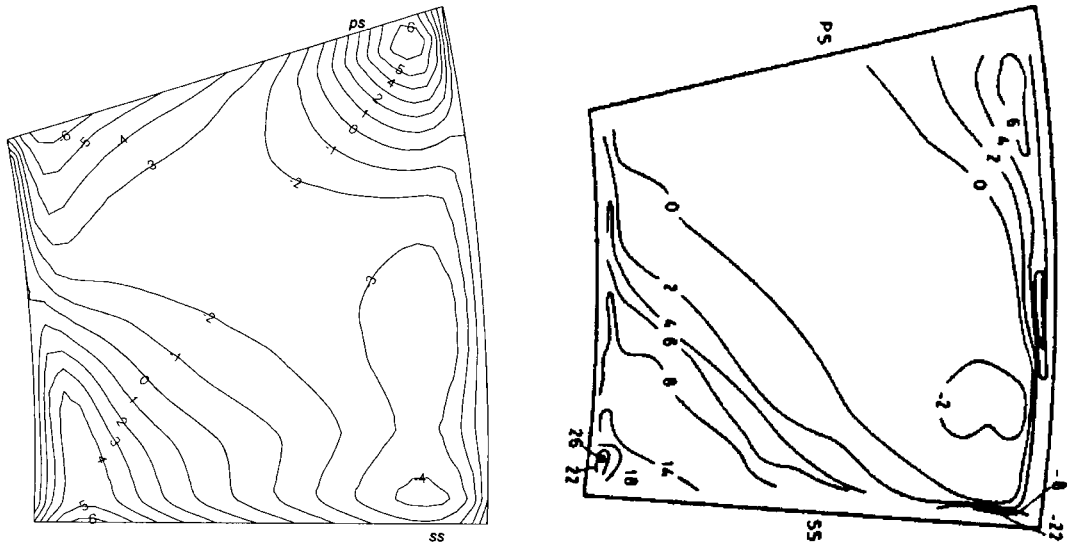

(b) x/c_{Ax} = 0.86 Computational Experimental [4]

Figure 15. Contour plots of flow angle γ at various measurement planes.

agreement with experimental test case results [4] and earlier numerical calculations [7] can be observed.

7.2.4. Total pressure loss results. The total pressure loss coefficient has also been calculated (Figure 12). Since the present solution is inviscid, the only physical loss is the one introduced by the inlet total pressure profile. Thus, some differences are expected from the 'viscous' experimental results. The computational maximum total pressure loss is as high as 20% of the

experimental result. The main source of this discrepancy is due to discretization errors, grid distortions at the leading and trailing edges and high turning. The test case was run twice with uniform and non-uniform inlet profiles. Grid, numerical smoothing and exit boundary

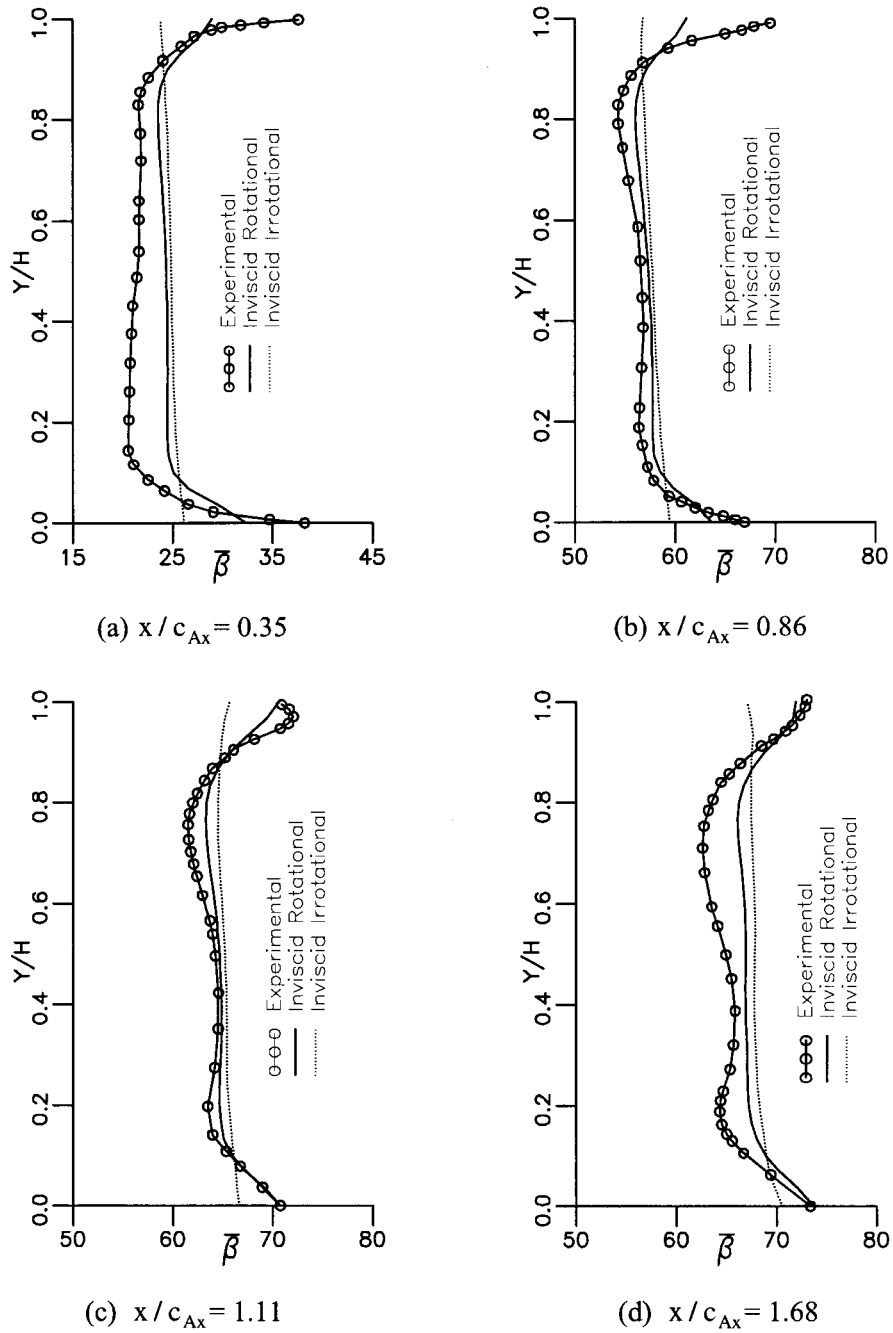

Figure 16. Radial distribution of the pitchwise averaged β flow angle at various measurement planes.

conditions were the same. By subtracting the total pressure of the irrotational results from the rotational one, an attempt to remove the numerical uncertainty was made. The result obtained using the techniques described above is in close agreement with experimental data [4].

7.2.5. Secondary velocities. On the blade suction side, both legs of horse-shoe vortices can be distinguished (Figure 13(a)). The horse-shoe vortices interact with counter rotating passage vortices at the downstream. Two of the vortex cores are located near the hub and cover slightly less than the half span. The other two are located in the upper half of the blade passage. At the pressure side, the horse-shoe vortex leg rotates in the same direction as the passage vortex and therefore, both have coalesced (Figure 13(a) and (b)). These two separate, but interacting, secondary flow mechanisms have also been the focus of different researchers: Boletis *et al*. [4] investigated skewed inlet boundary layer type flow profiles through the VKI turbine nozzle, while highly three-dimensional blade passage loading has been addressed by Arts [6], who considered a tip endwall contoured VKI annular turbine nozzle guide vane.

7.2.6. Flow angle results. In the figures that follow, the flow angle β is taken to be indicated as positive when pointing from pressure side to suction side. The radial flow angle γ is positive when pointing from hub to tip.

At $x/c = 0.35$ (Figure 23(a)), the horse-shoe vortex influence on the blade passage flow become noticeable. The downwash angle γ at the pressure side hub endwall corner reaches $-4°$ and a corresponding upward motion is seen at the pressure side tip endwall reaching to 4°. Flow angle β variation also depends both on the incoming endwall boundary layers and on the transverse pressure gradient across the blade passage. The computational and experimental flow angle β contours are given in Figure 14(a) and (c). Flow angle β contours at $x/c = 0.35$ (Figure 14(a)) show the clockwise rotating strong vortex at the blade suction side and at the 1/4 pitch of the blade passage endwall regions. The endwall flow angle β gradients are less pronounced in the computational results (Figure 14(b)). Further downstream the computed core flow has a uniform flow angle β of 68°, while in the experiment a non-uniform smaller turning is observed (Figure 14(c)). As the flow proceeds further downstream, the radial flow angle γ variations near the hub strengthen (Figure 15(a) and (b)).

7.2.7. Spanwise distribution of the pitch average flow angle results. The axial evolution of the pitchwise averaged flow angle β is given in Figure 16(a)–(d). The characteristic over/under-turning behavior of the flow under the influence of secondary flows has been successfully captured. In Figure 16(a) and (c), larger differences between computational and experimental pitchwise averaged flow angle $\bar{\beta}$ profiles are observed. In the computation, the no-slip boundary condition at the blade surface causes a high turning, while in the experiment the viscous flow around the blade leading and trailing edges give a smaller turning angle. Closer agreements are observed within the confined blade passages. Underturning and overturning near the endwall are less pronounced in the calculation. This suggests the presence of other vortical motion related to local viscosity and blade boundary layer. Overall, the pitch averaged results produced in this work seem to be in good agreement with the experimental spanwise pitch averaged flow angle β distribution [4,5].

8. CONCLUSION

An Euler solver for three-dimensional internal flow has been presented. A cell vertex finite volume method has been applied to a highly bent duct and to an annular turbine blade passage

with high turning. It has been possible to calculate the development of the inviscid secondary flow generated by the presence of an inlet total pressure gradient. The development of full passage vortex and streamwise bending of horse-shoe vortices have been shown to lead to secondary flows. Agreement has been obtained with the available experimental and computational data. It is concluded that the present code is capable of quantitatively reproducing the physics of the complex vortex structures.

ACKNOWLEDGMENTS

Authors would like to thank Nuri Çarkoğlu for the grid generation of the nozzle vanes of the VKI low-speed turbine facility using the IDEAS™ package and to Dr. Sieverding for providing the VKI low-speed turbine test case.

APPENDIX A. NOMENCLATURE

a	speed of sound (non-dimensionalized with the stagnation speed of sound)
c	chord length
c_{Ax}	axial cord length
C_{ps}	static pressure coefficient.
C_{p0}	total pressure coefficient.
e	total energy per unit volume
F, G, H	flux terms
h	blade height
n	normal vector
p	pressure
R	radial direction
Q	state vector
t	time
u, v, w	Cartesian components of non-dimensional velocity vector non-dimensionalized with the stagnation speed of sound
V	non-dimensional absolute velocity, $V=\sqrt{u^2+v^2+w^2}$
x, y, z	Cartesian co-ordinates
β	pitchwise flow angle
γ	radial flow angle
μ	numerical smoothing coefficient
σ	numerical smoothing parameter
θ	tangential direction
ρ	density
Ω	control volume
$\partial\Omega$	closed surface around control volume
Δt	time step
ΔV	volume of cell

Subscripts

c	cell index
FS	free stream
m	node index
R	radial direction

x, y, z	components in co-ordinate directions
Y	axial direction
s	static quantity
0	total quantity
1	inlet
2	outlet

Superscript

n	time step index
–	pitchwise average
=	pitchwise and spanwise average

APPENDIX B. EXPRESSIONS FOR SURFACE AREA VECTORS OF FINITE VOLUME CELLS

$$\vec{S}_1 = \frac{1}{2}(\vec{r}_1 - \vec{r}_3) \times (\vec{r}_4 - \vec{r}_2) \quad \vec{S}_3 = \frac{1}{2}(\vec{r}_4 - \vec{r}_5) \times (\vec{r}_1 - \vec{r}_8) \quad \vec{S}_5 = \frac{1}{2}(\vec{r}_2 - \vec{r}_5) \times (\vec{r}_6 - \vec{r}_1)$$

$$\vec{S}^2 = \frac{1}{2}(\vec{r}_7 - \vec{r}_5) \times (\vec{r}_6 - \vec{r}_8) \quad \vec{S}_4 = \frac{1}{2}(\vec{r}_7 - \vec{r}_2) \times (\vec{r}_6 - \vec{r}_3) \quad \vec{S}_6 = \frac{1}{2}(\vec{r}_3 - \vec{r}_8) \times (\vec{r}_7 - \vec{r}_4)$$

All these vectors point outwards (Figure 1).

APPENDIX C. EXPRESSIONS FOR ΔF, ΔG, ΔH

$$\Delta Q = \begin{bmatrix} \Delta\rho \\ \Delta(\rho u) \\ \Delta(\rho v) \\ \Delta(\rho w) \\ \Delta(e) \end{bmatrix} \qquad \Delta F = \begin{bmatrix} \Delta(\rho u) \\ u\Delta(\rho u) + u\rho\Delta u + \Delta p \\ v\Delta(\rho u) + u\rho\Delta v \\ w\Delta(\rho u) + u\rho\Delta w \\ h_0\Delta(\rho u) + u\rho\Delta h_0 \end{bmatrix}$$

$$\Delta G = \begin{bmatrix} \Delta(\rho v) \\ u\Delta(\rho v) + v\rho\Delta u \\ v\Delta(\rho v) + v\rho\Delta v + \Delta p \\ w\Delta(\rho v) + v\rho\Delta w \\ h_0\Delta(\rho v) + v\rho\Delta h_0 \end{bmatrix} \qquad \Delta G = \begin{bmatrix} \Delta(\rho w) \\ u\Delta(\rho w) + w\rho\Delta u \\ v\Delta(\rho w) + w\rho\Delta v \\ w\Delta(\rho w) + w\rho\Delta w + \Delta p \\ h_0\Delta(\rho w) + w\rho\Delta h_0 \end{bmatrix}$$

$$\Delta p = (\gamma - 1)\left\{\Delta e - \frac{1}{2}[u\Delta(\rho u) + v\Delta(\rho v) + w\Delta(\rho w) + \rho u\Delta u + \rho v\Delta v + \rho w\Delta w]\right\}$$

$$\rho\Delta u = \Delta(\rho u) - u(\Delta\rho) \qquad \rho\Delta v = \Delta(\rho v) - v(\Delta\rho) \qquad \rho\Delta w = \Delta(\rho w) - w(\Delta\rho)$$

$$h_0 = (e + p)/\rho \qquad \rho\Delta h_0 = \Delta e + \Delta p - h_0\Delta\rho$$

REFERENCES

1. L.A. Povinelli, 'Assessment of three-dimensional inviscid codes and loss calculations for turbine aerodynamic computations', *ASME 84-GT-187*, 1984.
2. C.H. Sieverding, 'Secondary flows in straight and annular turbine cascades', In A.S. Üçer *et al.* (eds.), *Thermodynamics and Fluid Mechanics of Turbomachinery*, Vol. 2, NATO ASI Series, Series E: Applied Sciences, 1984, No.97.
3. C.H. Sieverding, W. Van Hove and E. Boletis, 'Experimental study of the flow field in an annular turbine nozzle guide vane', *ASME 83-GT-120*, 1983.
4. E. Boletis, C.H. Sieverding and W. Van Hove, 'Effects of a skewed inlet endwall boundary layer on the 3D flow field in an annular turbine cascade', *AGARD-CP-351*, *Paper 16*, 1983.
5. C.H. Sieverding, 'Test case E/TU-1: low speed annular turbine blade row', *AGARD-AR-275*, *Propulsion and Energetics Panel Working Group 18 on Test Cases for Computation of Internal Flows in Aero-Engine Components*, 1990, pp. 322–323.
6. T. Arts, 'Effects of endwall contouring on the three-dimensional flow field in an annular turbine nozzle guide vane part 2—numerical investigation', *ASME 85-GT-108*, 1985.
7. W. Van Hove, 'Calculation of three-dimensional, inviscid, rotational flow in axial turbine blade rows', *J. Eng. Gas Turbines Power*, **106**, 430–436 (1984).
8. O. Novak, O. Schafer, B. Schönung and H. Patzold, 'Use of advanced CFD codes in the turbomachinery design process', *ASME-92-GT-324*, 1992.
9. E. Oktay, S. Akmandor and A.S. Üçer, 'Three-dimensional solution of internal flows using a cell vertex finite volume method', *AGARD-CP-510*, 1991, Paper 27.
10. E. Oktay, 'A cell vertex method for 3D inviscid internal flows', *Ph.D. Thesis*, M.E.T.U., Ankara, Turkey, 1991.
11. R.H. Ni, 'A multiple-grid scheme for solving the Euler equations', *AIAA J.*, **20**, 1565–1571 (1982).

